


Article

ZnO/rGO/ZnO Composites with Synergic Enhanced Gas Sensing Performance for O₃ Detection with No Ozonolysis Process

Rayssa Silva Correia, Amanda Akemy Komorizono, Julia Coelho Tagliaferro, Natalia Candiani Simões Pessoa and Valmor Roberto Mastelaro * 

Institute of Physics of São Carlos, University of São Paulo, São Carlos 13566-590, SP, Brazil; rayssa.sc@usp.br (R.S.C.); amanda.akemy@usp.br (A.A.K.); julia.tagliaferro@usp.br (J.C.T.); taliacandiani@usp.br (N.C.S.P.)

* Correspondence: valmor@ifsc.usp.br

Abstract

rGO/ZnO composites have been widely studied for use as toxic gas sensors due to the synergistic effect between the materials and the reduction in sensor operating temperature promoted by rGO. However, few studies have employed rGO/ZnO sensors for ozone detection, as graphene materials are oxidized and/or degraded when exposed to ozone. This paper reports on a study of ZnO/rGO/ZnO-based sensors with different ZnO NP morphologies for ozone sensing. ZnO nanoparticles with needle-like and donut-like morphologies were synthesized by the precipitation method, and bare ZnO and ZnO/rGO/ZnO composite sensors were fabricated by layer-deposition of ZnO and/or rGO via drop-casting, forming a “sandwiched” structure that protects the rGO sheets. Bare ZnO and ZnO/rGO/ZnO composites were analyzed by varying the temperature from 200 to 300 °C. The ZnO/rGO/ZnO sensor provided a high 13.3 response ($R_{\text{gas}}/R_{\text{air}}$) and recovery times of 442 s and 253 s, respectively, for 50 ppb of O₃, as well as high selectivity to ozone gas compared to CO, NH₃, and NO₂ gases. No oxidation or degradation of the sensor was observed during ozone detection measurements, indicating that the adopted manufacturing methodology was successful.

Keywords: gas sensors; ozone detection; ZnO-rGO-ZnO sensors

1. Introduction

Air pollution significantly impacts human health, the environment, and ecosystems, and is considered the fourth-leading risk factor for premature death. In this context, the progressive industrialization of society and the growing need for environmental protection have increased demand for gas sensors [1]. However, the development of gas-sensing devices with high responsivity, good stability and repeatability, and excellent selectivity has remained challenging; therefore, the development of faster, more selective, highly sensitive, and low-cost gas sensors is mandatory.

Ozone (O₃), an allotrope of oxygen with high chemical reactivity and strong oxidizing capacity, is an alarming air pollutant. It plays a fundamental role in absorbing ultraviolet radiation from the sun and has broad applicability in the industrial sector as a sanitizing agent and in biomedicine as a fungicide and bactericide [2,3]. However, prolonged exposure to specific concentrations of ozone can cause several harmful effects on human health, ranging from airway irritation to reduced lung capacity [4]. The World Health Organization (WHO) recommends an O₃ exposure limit of 50 ppb for an 8 h journey to avoid permanent



Received: 6 November 2025

Revised: 19 December 2025

Accepted: 26 December 2025

Published: 1 January 2026

Copyright: © 2026 by the authors.

Licensee MDPI, Basel, Switzerland.

This article is an open access article

distributed under the terms and

conditions of the [Creative Commons](https://creativecommons.org/licenses/by/4.0/)

[Attribution \(CC BY\)](https://creativecommons.org/licenses/by/4.0/) license.

health damage [5]. Therefore, sensors capable of detecting that gas quickly, reliably, and cost-effectively, given its extensive applicability and associated risks, must be developed.

Chemiresistive sensors based on metal oxide semiconductors (MOSs) such as zinc oxide (ZnO) [5,6], nickel oxide (NiO) [7], tin oxide (SnO₂) [8,9], tungsten oxide (WO₃) [10,11], and indium oxide (In₂O₃) [12] have been extensively studied in recent decades for ozone detection due to their fast response time and low cost [13–15]. Among MOSs, zinc oxide (ZnO), an n-type semiconductor with a 3.3 eV bandgap, high electrical mobility (60 meV), and thermal stability, has been widely applied as a gas sensor [16,17]. Depending on the parameters and methods used in its synthesis, ZnO can exhibit a variety of morphologies, with smaller structures associated with greater reactivity [18,19]. Several studies have focused on ZnO-based sensors for ozone detection [6,20]. However, the main disadvantages of bare ZnO are its low sensitivity, cross-sensitivity to other interfering gases, and higher operating temperature [16,21]. Those limitations can be addressed through different approaches, such as surface modification, inclusion of noble catalytic metals, elemental doping, and formation of multicompositional structures, including p-n junctions [16,22].

Reduced graphene oxide (rGO) is a p-type semiconductor which is highly promising for sensor fabrication due to its high specific surface area (2630 m² g⁻¹), high carrier mobility (~230,000 cm² V⁻¹ s⁻¹), good mechanical properties, low production cost, and good gas adsorption capacity [1,23]. The presence of residual oxygen functional groups on its surface provides additional reactive sites for gas adsorption [22]. However, pristine rGO shows low sensitivity, and rGO/MOS has been widely investigated to improve the response, selectivity, and stability of devices [1,22]. The combination of ZnO, a good electron donor, with rGO, a good electron acceptor, induces the formation of a p-n or n-p junction. This interaction has been shown to enhance the sensing properties of ZnO for detecting multiple gases, including NH₃ [16,24], NO₂ [25,26], H₂S [27], and CO₂ [28]. On the other hand, only a few studies [29–31] have explored the rGO/ZnO combination for monitoring that gas due to the rapid degradation of graphene-based materials in the presence of O₃ [32]. Our previous study [31] was devoted to the development of a methodology based on a ZnO/rGO/ZnO “sandwich” for ozone detection without oxidation or degradation of the sensor, thus paving the way for investigations and the development of various MOS/rGO/MOS-based sensors for ozone detection.

This paper reports on a study of ZnO/rGO/ZnO sensors with two different morphologies of ZnO nanoparticles for ozone detection. ZnO NPs with donut-like and needle-like morphologies were synthesized by the precipitation method, and ZnO/rGO/ZnO sensors were fabricated by depositing ZnO and rGO layers according to the drop-casting method, forming a “sandwich” structure. The sensing properties of bare ZnO devices and their composites were evaluated for ozone gas detection. ZnO/rGO/ZnO-based sensors showed no oxidation or degradation in the presence of ozone, indicating that the adopted synthesis method was successful. Among the sensors, the ZnO/rGO/ZnO needle-like sensors showed high response and selectivity to ozone gas.

2. Materials and Methods

2.1. Synthesis of ZnO Nanoparticles

As reported in our previous paper [33], ZnO with needle-like and donut-like morphologies was obtained by a precipitation method, using zinc acetate and ammonium hydroxide as the precursor and precipitating agent, respectively. An aqueous solution of 0.3 M zinc acetate was prepared for the needle morphology, and the synthesis was conducted at room temperature, whereas a 0.15 M solution of zinc acetate in ethanol was used for the donut morphology, with a 100 °C synthesis temperature. For both morphologies, the mixtures were maintained under continuous magnetic stirring at 1200 rpm, and ammonium

hydroxide was added with a pipette until the system reached pH 8.8 for the needle-like morphology and 8.0 for the donut morphology.

After adjusting the pH of the solutions, a light gray precipitate formed and aged for 8 days to ensure crystal growth. The sediments were then subjected to washing, drying, and heat treatment processes to control the characteristics of the colloidal particles present in the dispersions. The precipitate containing needle-shaped particles was washed with distilled water, and the sample containing donut-shaped particles was washed with ethanol, both under mechanical agitation. The samples were then dried at 100 °C and subsequently heat-treated for 2 h at 300 °C. The heat treatment was performed to eliminate any traces of the solvents used during synthesis and has no impact on the crystal structure or morphological characteristics.

2.2. Sensor Manufacturing

A solution of 10 mg/mL of ZnO in ethanol and a dispersion of 2 mg/mL of commercial reduced graphene oxide in milli-Q water were prepared for the manufacturing of pure ZnO sensors and ZnO-rGO-ZnO composites. The dispersion of rGO synthesized with poly(4-styrenesulfonate sodium) at a concentration of 10 mg/mL was acquired from Sigma Aldrich. Five 10 μ L layers of the ZnO solution were deposited onto platinum-integrated electrodes by drop-casting for the needle and donut ZnO sensors, as shown in Figure 1a. The methodology previously reported by our research group was adopted for the ZnO-rGO-ZnO needle and donut sensors [31]. Initially, a 10 μ L layer of the ZnO suspension was deposited on the interdigitated electrode, followed by a 10 μ L layer of the rGO dispersion and another three layers of the ZnO suspension, forming a “sandwich” (see Figure 1b).

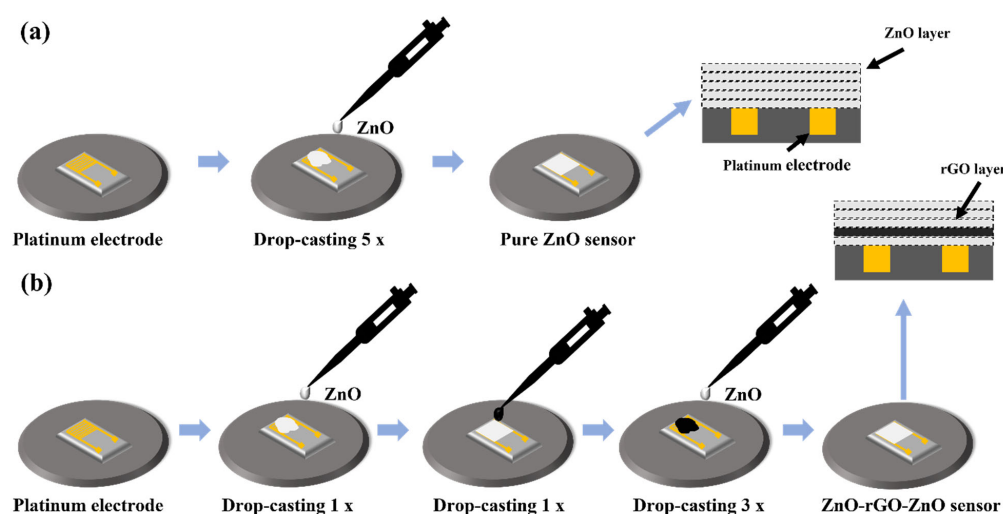


Figure 1. Procedure for the fabrication of sensors of (a) pure ZnO and (b) ZnO-rGO-ZnO.

2.3. Gas Sensor Measurements

The experimental apparatus used for gas detection measurements was built by NaCA group and the baseline was obtained with the use of synthetic air (reference gas consisting of 20% oxygen and 80% nitrogen) at a 100 mL/min constant flow rate. The sensors were heated by a hotplate located within the gas detection system for measurements at different operating temperatures (200, 250, and 300 °C). Two gold-coated tungsten needles applied a 1 V voltage to the electrodes and a Keithley electrometer measured the electrical resistance of the film.

A UVP lamp (model P/N 90-0004-01, Germany), located along the path of the reference gas inside a closed chamber, produced ozone gas, whose concentration was monitored by a commercial sensor (ATI F123513-00-1388, Colleagueville, PA, USA). The gas system used is

shown in Figure S1 of the Supplementary Data. The NO_2 and NH_3 gases were generated via permeation tubes in an Owlstone V-OVG system (Darien, CT, USA), which controls gas concentration based on permeation rate as a function of temperature. Finally, a CO gas cylinder was used for the CO detection measurements. The sensors were exposed to the target gases for 10 min with a 15 min interval between exposures for sensor recovery in all measurements.

2.4. Characterization

The structural characterization of the synthesized ZnO powders was performed using X-ray diffraction (XRD). The diffractometer used was a Rigaku Ultima IV (Japan) with $\text{Cu-K}\alpha$ radiation ($\lambda = 1.5418 \text{ \AA}$) and a LiF monochromator (100), and the diffractograms were obtained using the conventional configuration (θ – 2θ). Raman spectroscopy, conducted under a Witec microscope (Ulm, Germany) equipped with a Nikon objective lens ($100\times$, $\text{NA} = 0.9$) and an Ar laser (514 nm), was used to characterize the structure of reduced graphene oxide (rGO), and PeakFit 1.49v software processed the data. Photoluminescence measurements were made using a 355 nm laser (Cobolt/Zouk, Germany) for excitation in a 20 cm spectrometer (AndorKymera, Northern Ireland). The band gap of the samples was estimated using the Tauc plot method based on diffuse reflectance spectra obtained with a Shimadzu UV-2600 Plus spectrophotometer (Japan) over 220–850 nm.

The morphological characterization of ZnO particles, rGO, and composites was conducted using scanning electron microscopy (SEM), and SEM images were obtained with a ZEISS SIGMA microscope (Germany) equipped with a field-emission electron gun (FESEM). X-ray excited photoelectron spectroscopy (XPS) was used for compositional characterization of the surface of ZnO and the ZnO-rGO-ZnO composite, and measurements were performed on a Scienta Omicron ESCA+ spectrometer (Germany) with 1486.7 eV monochromated Al-K α radiation, 280 W incident power, and a charge neutralizer. CasaXPS Version 2.3.27PR4.4 software, calibrated by the energy of adventitious carbon (284.8 eV), processed the spectroscopy data.

3. Results and Discussion

3.1. Structural Characterization

Figure 2a shows the diffraction pattern of ZnO samples with donut-like and needle-like morphologies. The diffraction peaks of both samples are associated with the hexagonal close-packed wurtzite-type crystal structure of ZnO, as per the 36-1451 crystallographic record JCPDS [34]. No peaks indicating a second phase or impurity were detected in the samples. Since the rGO layer is under three layers of ZnO, the characteristic peak ($2\theta = 10$ – 11°) of the material does not appear in the diffractogram [35]. However, the diffractograms of the composites are shown in Figure S2 of the Supplementary Data. Since the samples were deposited on a Si substrate, the characteristic Si peak was detected around $2\theta = 33$ – 34° . Raman spectroscopy is a non-destructive tool widely used to characterize carbon materials, such as graphene, reduced graphene oxide, and carbon nanotubes. Figure 2b,c shows the Raman spectra of ZnO-rGO-ZnO composites with donut-like and needle-like morphologies. The Raman spectrum of rGO is displayed in Figure S3 of the Supplementary Data. Peaks represented by letters refer to the characteristic peaks of rGO—the main ones are those associated with D ($\sim 1350 \text{ cm}^{-1}$), G ($\sim 1580 \text{ cm}^{-1}$), and 2D ($\sim 2700 \text{ cm}^{-1}$) bands. The G band originates from the in-plane C–C sp^2 stretching vibration and corresponds to the doubly degenerate vibration mode (E_{2g}) of the phonons in the center of the Brillouin zone [36,37]. The D band is related to defects in the crystal lattice, i.e., any imperfection in the regular periodic arrangement of atoms [38]. The 2D band, or G' , is a second-order band that appears in the spectrum whenever sp^2 rings are present and is related to the electronic structure of

the graphene band. It is the overtone of the D band, i.e., it has twice its vibration frequency, but, unlike the latter, it is independent of the presence of defects [36,37]. The I_D/I_G ratio represents the defect density of rGO, and $I_D/I_G < 3.5$ indicates the material has a low degree of disorder [39,40]. According to Cançado et al. [41], that ratio can also be used to estimate the crystallite size (L_a) (Equation (1)):

$$L_a(\text{nm}) = (2.4 \cdot 10^{-10}) \cdot \lambda_l^4 \cdot \left(\frac{I_D}{I_G}\right)^{-1} \quad (1)$$

where λ_l is the measurement of the wavelength of the laser used in Raman spectroscopy ($\lambda_l = 514 \text{ nm}$). The estimated I_{2D}/I_G ratio represents the extent of “graphenization”, i.e., the presence of long-range regions formed by aromatic sp^2 carbon rings, like pristine graphene [42]. Table 1 provides the values of I_D/I_G , I_{2D}/I_G , and L_a .

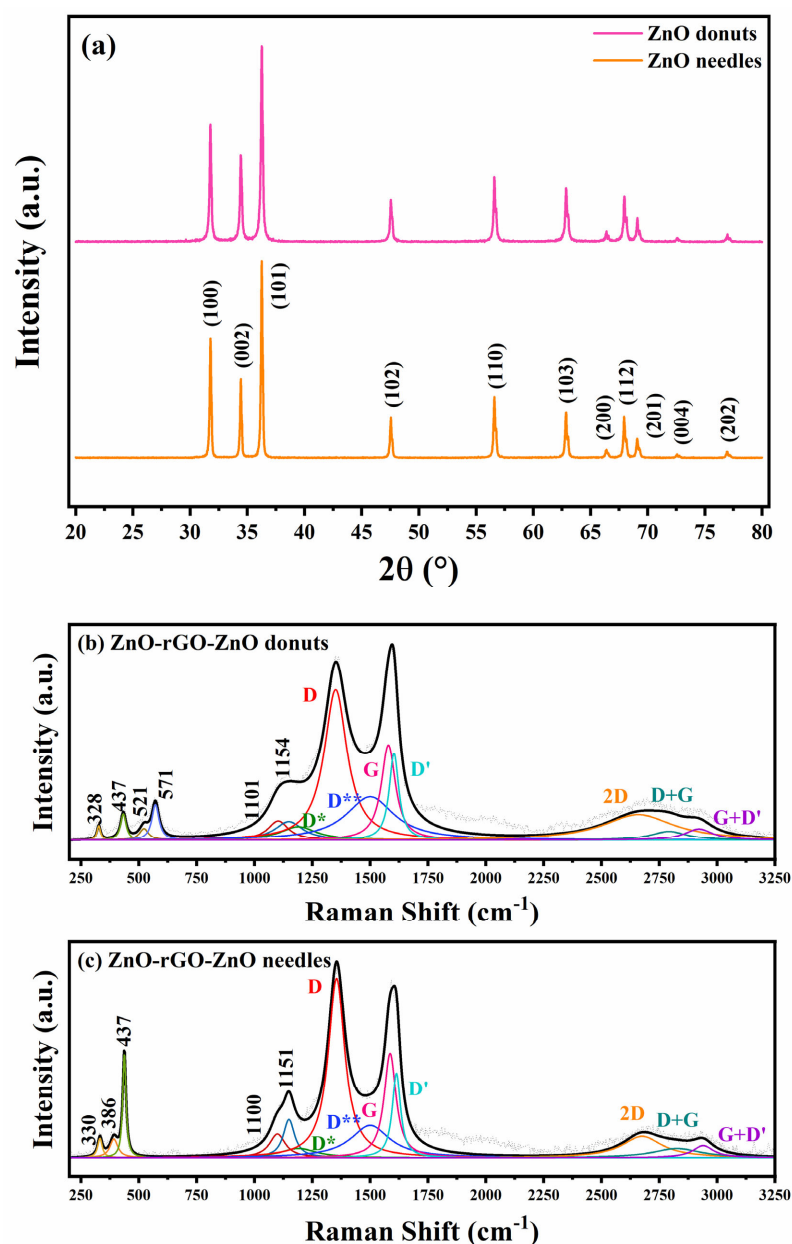


Figure 2. (a) Diffraction pattern of ZnO samples with needle and donut morphologies and (b,c) Raman spectrum of ZnO-rGO-ZnO composites with donut-like and needle-like morphologies, respectively.

Table 1. Data on I_D/I_G , I_{2D}/I_G , and L_a ratios obtained from the Raman spectra of rGO samples and ZnO-rGO-ZnO composites.

Sample	I_D/I_G	I_{2D}/I_G	L_a
rGO	1.84	0.15	9.12
ZnO-rGO-ZnO needles	1.72	0.21	9.75
ZnO-rGO-ZnO donuts	1.59	0.17	10.56

Apart from the characteristic peaks of rGO, Raman spectra also show peaks characteristic of the ZnO phase, as indicated by their positions in those spectra. The peak centered at 437 cm^{-1} corresponds to the vibrational mode of the $E_{2\text{high}}$ optical phonon, which is associated with vibrations of O atoms. The band centered at 571 cm^{-1} , which appears only in ZnO donuts, refers to longitudinal optical phonons $E_1(\text{LO})$ that are associated with defects such as oxygen vacancies or interstitial Zn atoms [43]. The peak located at 386 cm^{-1} , which appears only in ZnO needles, is attributed to the $A_1(\text{TO})$ mode [44]. Peaks $328\text{--}330\text{ cm}^{-1}$ and $1151\text{--}1154\text{ cm}^{-1}$ arise due to phonon scattering processes in the material [44,45]. The band at $328\text{--}330\text{ cm}^{-1}$ is attributed to the second-order dispersion of $E_{2\text{high}}\text{--}E_{2\text{low}}$ band phonons [44] and the one at $1151\text{--}1154\text{ cm}^{-1}$ has contributions from the $2A_1(\text{LO})$ and $2E_1(\text{LO})$ modes [45]. The ZnO spectrum also shows two second-order bands: one in the $540\text{--}700\text{ cm}^{-1}$ range and another in the $980\text{--}1200\text{ cm}^{-1}$ range. In both samples, only the band in the second range, i.e., $1100\text{--}1101\text{ cm}^{-1}$, was identified and is associated with $A_1(2\text{LO})$ optical combinations in the material [45]. The ZnO donut-like sample also shows a peak at 521 cm^{-1} , attributed to the Si substrate.

3.2. Optical Characterization

Photoluminescence spectroscopy (PL) is an effective technique for analyzing the effect of morphology on the electronic, optical, and photochemical properties of semiconductors such as ZnO [46]. In this study, the nature and density of structural defects in ZnO and ZnO-rGO-ZnO samples were investigated. The photoluminescence spectrum of ZnO typically consists of a near-UV band (luminescence edge) and a broad visible one (deep-level emission) [47]. Figure 3 displays the luminescence spectra of ZnO with needle and donut morphologies, and their composites, measured at 355 nm excitation wavelength at room temperature. The spectra show near-band-edge (NBE) emission around 391 and 393 nm for ZnO donut-like and needle-like, respectively. For the composites, this peak appears at 392 and 394 nm for ZnO-rGO-ZnO donuts and ZnO-rGO-ZnO needles, respectively. Due to the excellent electrical properties of rGO, an efficient transfer of charge carriers and a long lifetime of the photogenerated electron–hole pairs are expected [48]. This is evident in the reduction in NBE emission intensity in the composites, confirming efficient charge-carrier transfer and prolonged electron–hole-pair lifetimes. Such emission in the UV region is due to the recombination of free excitons via an exciton–exciton collision process [46], and its attenuation in ZnO donut-like structures suggests that the material has more defects and can trap free electrons and photogenerated holes [49].

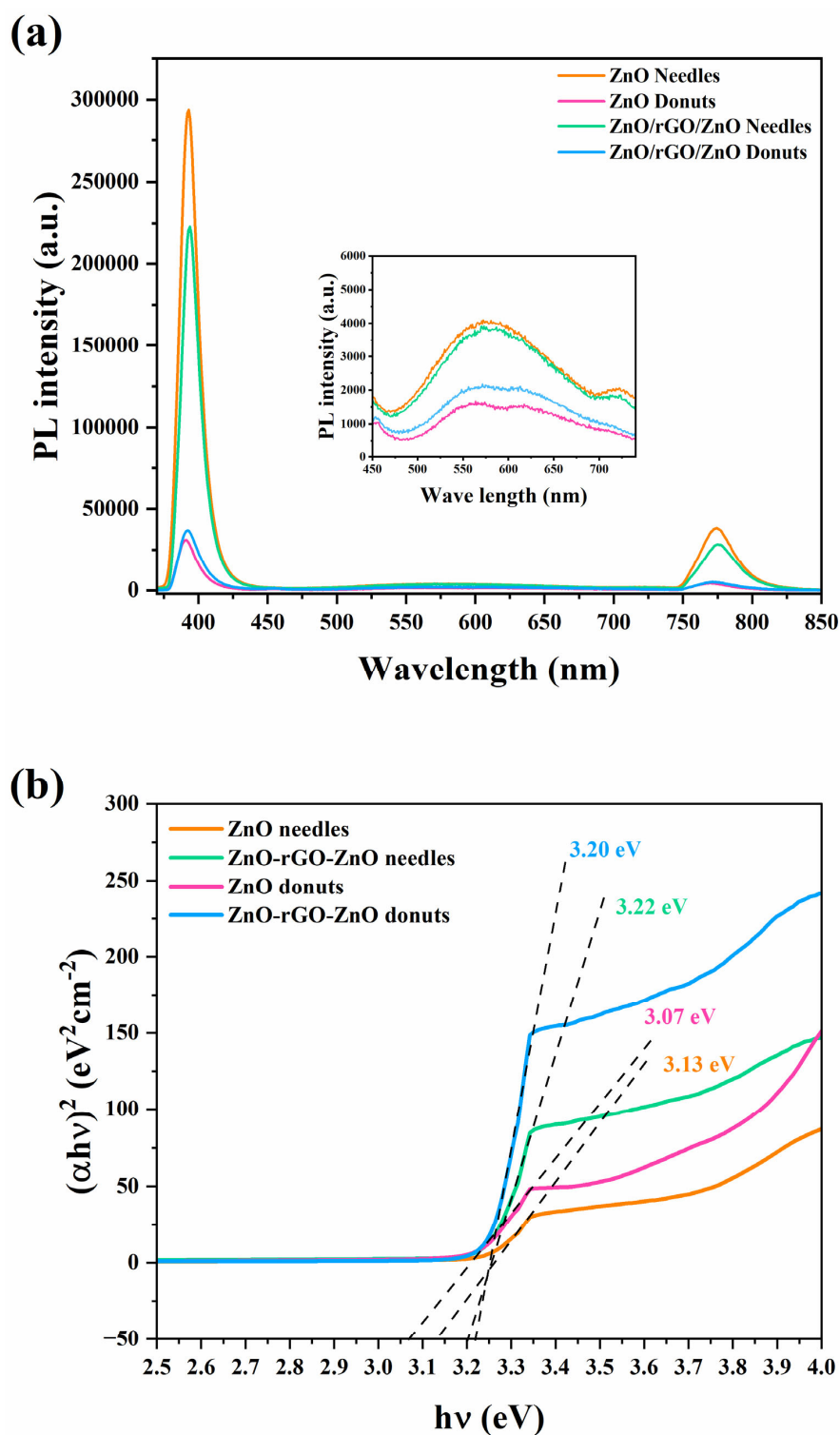


Figure 3. (a) PL spectrum and (b) plot of Tauc of the UV-Vis spectra of the samples of ZnO with needle and donut morphologies and their composites.

The emission in the visible region is generally attributed to the energy levels of structural defects in ZnO. Different defects (e.g., interstitial zinc (Zn_i), oxygen vacancies (V_O), acceptor states such as zinc vacancies (V_{Zn}), and oxygen interstitials (O_i)) can be found in the ZnO phase [47,49]. In both spectra, the visible emission occurs in the yellow-orange region, around 600–650 nm, and is caused by optical transitions from the lower part of the conduction band to the oxygen interstitial [49]. It is higher for ZnO donut NPs, suggesting a higher defect density than for ZnO needle NPs, corroborating the Raman

spectroscopy results. The emission around 760 nm is second-order diffraction from the spectrometer's diffraction grating relative to the ZnO peak around 380 nm.

Figure S4 shows the UV-Vis spectra of the ZnO needle and donut samples and their composites. The bandgap of the samples can be estimated using the Tauc plot and the Kubelka-Munk equation [50]:

$$(\alpha hv)^n = K(hv - E_g) \quad (2)$$

where hv is the photon energy, E_g is the bandgap energy, K is a constant dependent on energy, n depends on the nature of the transition, being 2 for a direct transition and $\frac{1}{2}$ for an indirect transition [50]. Figure 3b shows the Tauc plot for the samples. Through this figure, it was estimated that the bandgaps are 3.13 and 3.22 eV for ZnO needles and ZnO-rGO-ZnO needles and 3.07 and 3.20 eV for ZnO donuts and ZnO-rGO-ZnO donuts, respectively.

3.3. Morphological Characterization

Figure 4 shows FESEM images of ZnO needles, ZnO donuts, and their respective composites with rGO. The formation mechanism of long ZnO needles is attributed to the preferential growth of zinc oxide along the c -axis. This trend can be explained by analyses of the oxide's internal structure. Since anionic zinc $[\text{ZnO}(\text{OH})_4]^{2-}$ exists predominantly in basic conditions ($\text{pH} \sim 8.8$), upon the addition of ammonia to the solution, the anionic precursor is preferentially adsorbed by the positively charged face, i.e., face (0001), starting growth in the c -axis direction. The [0001] side also shows the highest growth rate; therefore, the initial length difference tends to increase throughout the synthesis, resulting in the observed needle-like morphology [19,51,52].

The mechanism of donut formation is related to the synthesis temperature and the solvent used. Given the synthesis temperature of the sample (100°C), which is higher than the boiling point of ethanol (78.4°C), the visible porosity of the structures can be attributed to rapid solvent evaporation during synthesis. The ethanolic medium is also responsible for the dehydration of zinc hydroxide formed from the precipitation of Zn^{2+} ions by OH^- ions, leading to the production of ZnO. The depression observed at the center of the particles is due to the pressure difference caused by the rapid decomposition of ethanol, leading to a donut appearance [19].

Figure 4c,d displays FESEM images of ZnO-rGO-ZnO composites for needles and donut morphologies, respectively. FESEM images of rGO are shown in Figure S5 in the Supplementary Data. It is well known that ozone is used to re-oxidize the surface of graphene oxide (GO) by introducing oxygenated functional groups between its sheets. The process, known as ozonolysis, causes oxidation and subsequent degradation of graphene-based materials, including GO and rGO. It is a thermally active process, and the successive exposure of rGO-based sensors to ozone gas causes their permanent degradation, thus impairing both their sensing properties and their application as ozone gas sensors [32,53]. Our group has previously reported that SMO/rGO/SMO-based sensors in the form of "sandwiches" prevent the ozonolysis process from degrading them [31]. Consequently, the objective of depositing ZnO-rGO-ZnO layers to form a "sandwich" is to protect rGO from exposure to ozone. Figure 4c,d shows that the rGO sheets are completely covered by ZnO NPs in both composites. Figure 4e shows a cross-sectional image of the ZnO/rGO/ZnO needles sensor, where the formation of the "sandwich" structure with rGO sheets between the layers of ZnO needle NPs can be observed. Figure 4f shows an enlargement of Figure 4e in which the rGO sheets between the NPs can be observed in more detail. Figure 4g shows a cross-sectional image of the ZnO/rGO/ZnO donut sensor. As with the ZnO/rGO/ZnO needle composite sensor, the rGO layer is sandwiched between the layers of ZnO donut

NPs, and its surface is completely covered. Figure 4h shows an enlargement of Figure 4g, showing the layers of the ZnO/rGO/ZnO “sandwich” in more detail. Through cross-sectional images, the thickness of both sensors was calculated to be $24.1 \pm 0.5 \mu\text{m}$ and $6.8 \pm 0.3 \mu\text{m}$ for ZnO/rGO/ZnO needles and ZnO/rGO/ZnO donuts, respectively.

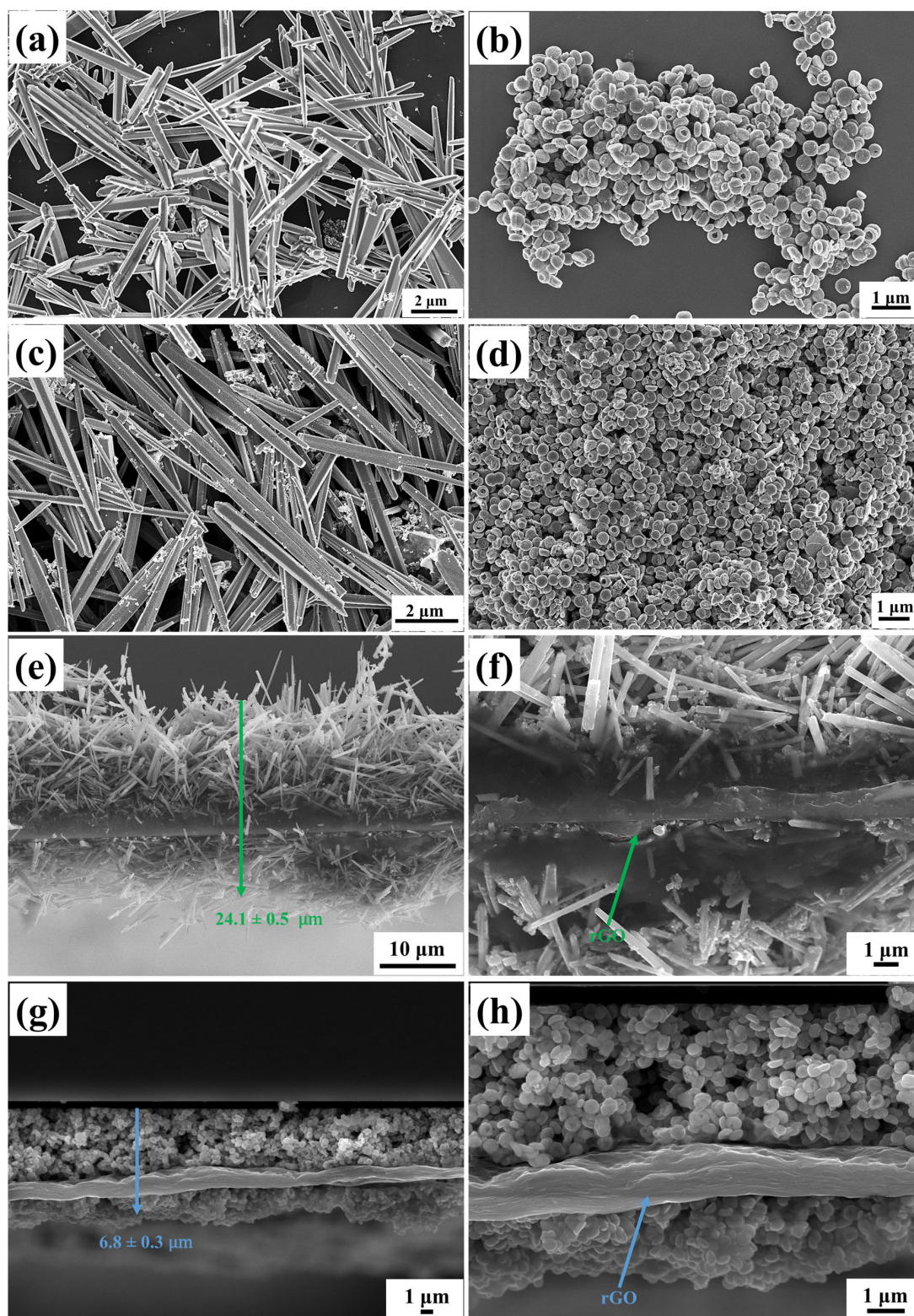


Figure 4. FESEM images of samples of (a) ZnO needles, (b) ZnO donuts, (c) ZnO/rGO/ZnO needles, and (d) ZnO/rGO/ZnO donuts and cross-section images of (e,f) ZnO/rGO/ZnO needles and (g,h) ZnO/rGO/ZnO donuts.

Figure S6 displays the particle size distribution of ZnO needle-like particles (0.27 μm average diameter and 4.96 μm average length) and ZnO donut-like particles (0.39 μm average diameter and 0.16 μm average width). Aspect ratios, calculated as ratios of particle length to thickness, were determined to be 18.4 for needle-like particles and 2.4 for donut-like ones.

3.4. Chemical and Surface Characterization

Figure 5 shows the survey spectrum of needle-like and donut-like ZnO nanoparticles, as well as their composites with rGO. The elements identified were C 1s (~285 eV), O 1s (~531 eV), and Zn (~1022 eV), with no impurities detected. Table 2 provides atomic percentage concentrations for each element and sample, indicating that the formation of the ZnO/rGO/ZnO composite resulted in increased carbon content in the samples, as expected.

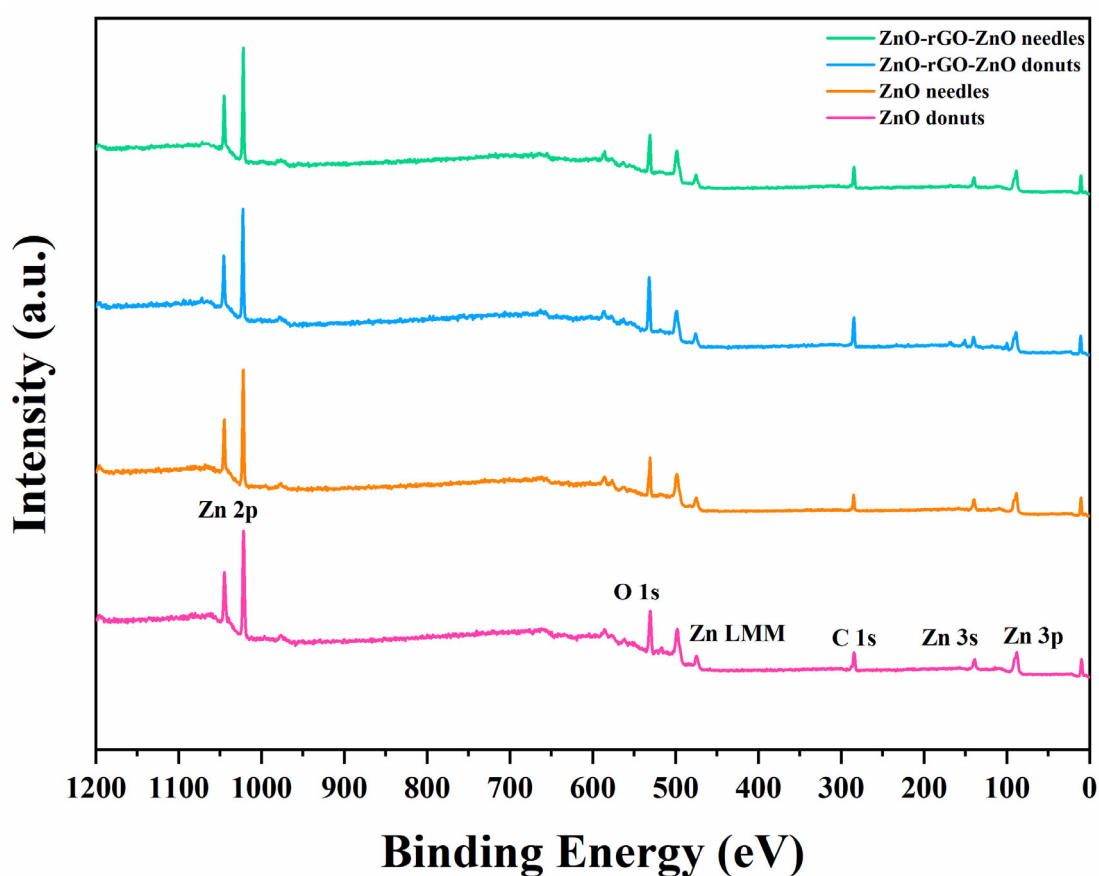


Figure 5. XPS survey spectrum of ZnO samples with needle and donut morphologies and their respective ZnO/rGO/ZnO composites.

Table 2. Surface composition of ZnO needle-like and donut-like samples and their respective composites.

Samples	C 1s (% at)	O 1s (% at)	Zn 2p (% at)
ZnO needle-like	43.29	45.42	11.29
ZnO donut-like	53.40	27.20	19.40
ZnO-rGO-ZnO needles	57.91	35.00	7.09
ZnO-rGO-ZnO donuts	56.63	38.09	5.28

Figure 6a–d shows the high-resolution spectra of the O 1s energy band for both pure ZnO and ZnO/rGO composites. The spectra were deconvoluted into three components, of which the first (~530 eV) is attributed to crystal lattice bonds between O^{2-} and Zn, the second (~531 eV) is related to bonds between oxygen and carbon, and the third is commonly associated with weakly adsorbed molecules [30,54]. Table 3 shows the concentration (%) for each element in the spectrum. The component related to O-C bonds in the composite samples is significantly increased, indicating that the carbon content in the samples has also increased. Figure S7 displays the high-resolution C 1s spectra of the composites.

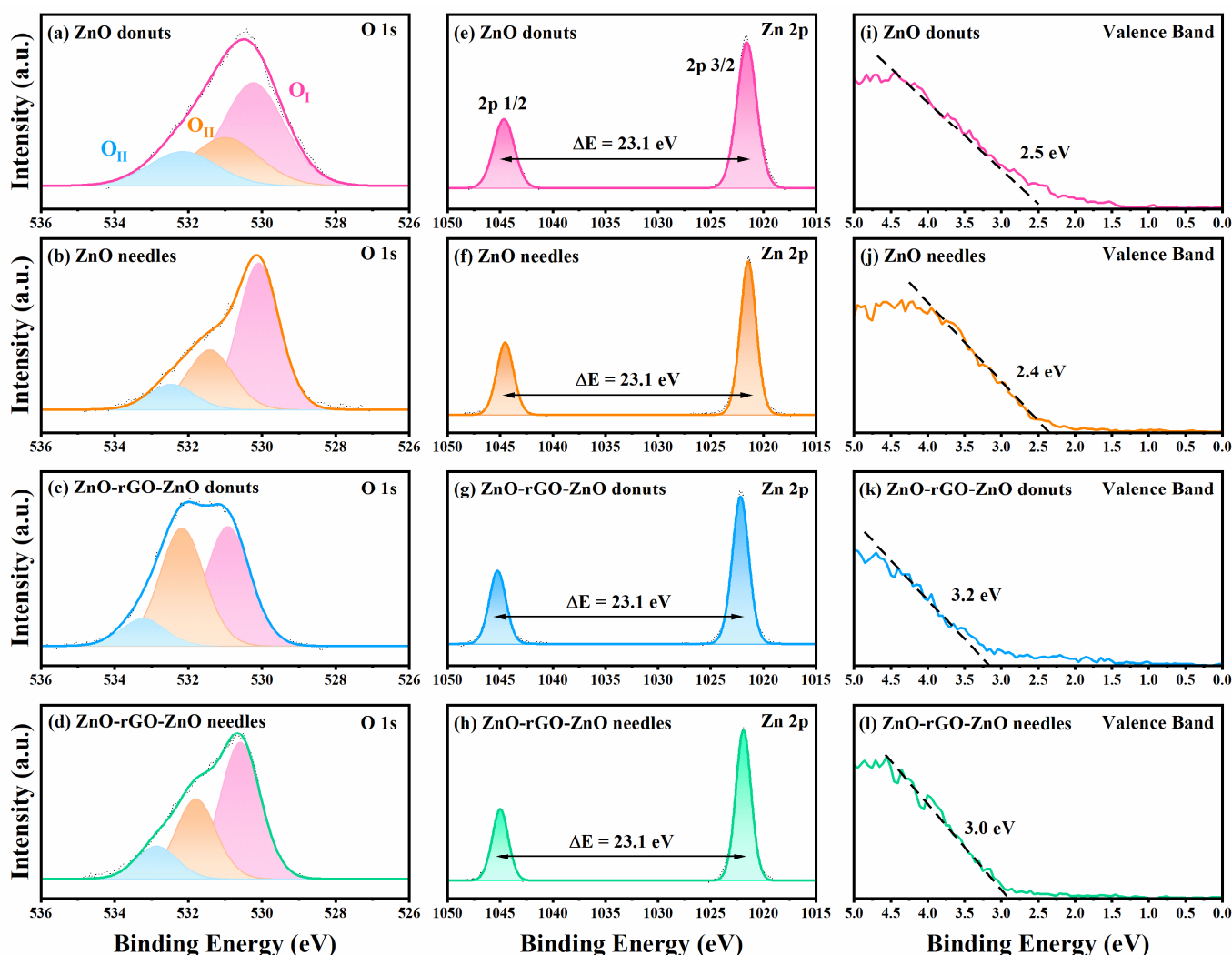


Figure 6. (a–d) High-resolution spectra of O 1s; (e–h) high-resolution spectra of Zn 2p and (i–l) valence bands of ZnO samples with needle-like and donut-like morphologies and their respective ZnO/rGO/ZnO composites.

Table 3. High-resolution O 1s spectral data of ZnO donut-like and needle-like samples and their respective composites.

Components	ZnO Donuts (% at)	ZnO/rGO/ZnO Donuts (% at)	ZnO Needles (% at)	ZnO/rGO/ZnO Needles (% at)
O _I	53.40	44.51	60.79	54.56
O _{II}	27.22	45.02	27.64	32.09
O _{III}	19.38	10.47	11.57	13.35

Figure 6e–h shows the high-resolution spectra of the Zn 2p band for the samples exhibiting a doublet spectral line with binding energies of approximately 1022 and 1045 eV for Zn 2p 1/2 and Zn 2p 3/2 transitions, respectively. The line is symmetrical and has $\Delta E = \sim 23$ eV [55]. The valence band energy maximum (VBE) of the samples was also measured by XPS analysis, as shown in Figure 6i–l. ZnO samples showed VBEs of 2.5 and 2.4 eV for donut-like and needle-like morphologies, respectively, whereas, in contrast, ZnO/rGO samples displayed higher values of 3.2 and 3.0 eV, respectively. Such valence-band energies are in good agreement with previously reported values for ZnO [56,57].

3.5. Gas Sensors

It is well known that the operating temperature of sensors significantly impacts their performance, as it affects the adsorption of oxygen species on the surface of materials [16]. ZnO and ZnO/rGO/ZnO sensors with needle and donut morphologies (Figures 7 and 8, respectively) were evaluated for O₃ gas at different temperatures to optimize the operating temperature of the devices. According to Figures 7a–c and 8a–c, when the sensors are exposed to O₃, an oxidizing gas, electrical resistance increases, which is a typical behavior of n-type semiconductors such as ZnO [17]. The same behavior occurs in the sensors of ZnO/rGO/ZnO composites (Figures 7d–f and 8d–f), as expected, since the sensors are composed mainly of ZnO with only one internal layer of rGO. After O₃ removal, the sensors' electrical resistance returns to baseline, indicating complete recovery. Furthermore, no oxidation or degradation of the sensors was observed when ZnO/rGO/ZnO composites were exposed to O₃, demonstrating that the adopted methodology successfully protected the rGO layer of the sensors and prevented damage during their application. To prove this, XPS measurements were performed before and after exposure of the ZnO-rGO-ZnO composite sensors, and the results are presented in Figures S8 and S9 in the Supplementary Data. Table S1, in the Supplementary Data, presents the data obtained from the spectrum survey of the sensors. It can be observed that the oxygen concentrations in the sensors do not show significant variation after exposure to ozone gas, confirming that rGO is not oxidized. Furthermore, the high-resolution C1s spectrum also shows no alteration with exposure of the sensors to the gas. Table S2 presents the concentrations of each component in atomic percentage.

Figure 9a shows a comparison of the response of ZnO needle and donut sensors when exposed to 50 ppb of O₃ at different temperatures (300, 250, and 200 °C). The operating temperature is reduced in both sensors, and their responses increase. However, the ZnO needle-like material shows a superior response across all temperatures, with 200 °C as the optimal sensor temperature. Those below 200 °C were not studied because the sensors did not fully recover after gas removal. The adsorption/desorption mechanism slows down as the temperature decreases in semiconductor metal oxide gas sensors. This is because the rate of these thermally activated processes diminishes due to the lower thermal energy of the gas molecules and adsorbed species [58]. It is well known that several factors, including morphology, particle size, aspect ratio, defects, crystallinity, and dimensionality, influence the sensing properties of materials. The dimensionality of the nanostructures directly affects the performance of MOS-based gas sensors; 1-D nanostructures have a higher surface area–volume ratio, thus displaying more active sites than 2-D and 3-D nanostructures. In addition, effective charge-carrier transport and high surface energy are other advantages of 1-D nanostructures for gas sensors. Such nanostructures also enable the nanostructure diameter to reach the Debye radius, thereby promoting the maximum change in the material's electrical resistance upon the adsorption of gas molecules [59]. Therefore, the ZnO needle sensor (1-D) shows a superior response compared to the ZnO donut sensor (3-D).

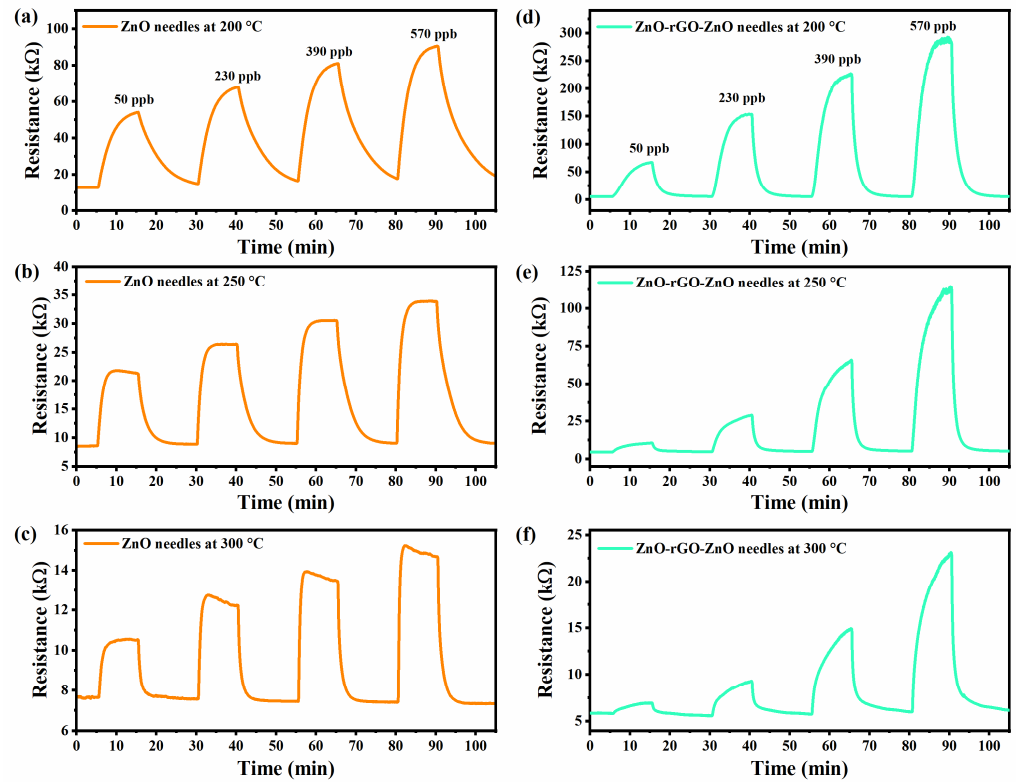


Figure 7. Dynamic response-recovery curves for O_3 of the ZnO needle sensor at (a) 200 °C, (b) 250 °C, and (c) 300 °C and of the ZnO donut sensor at (d) 200 °C, (e) 250 °C, and (f) 300 °C.

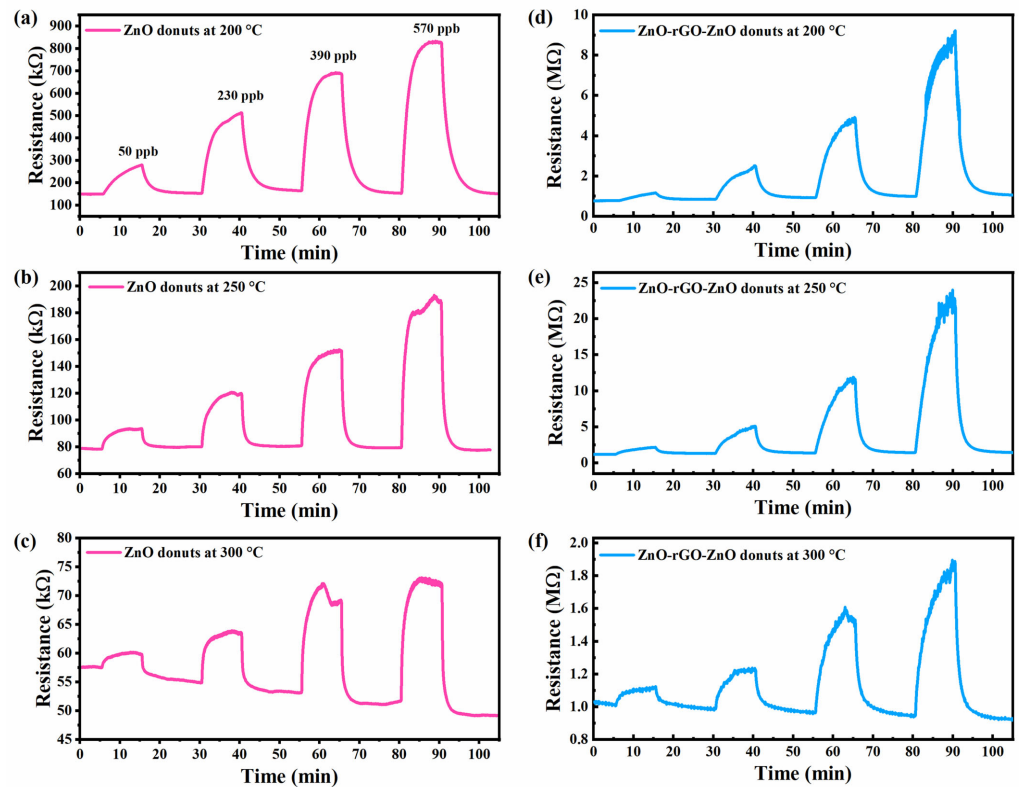


Figure 8. Dynamic response-recovery curves for O_3 of the ZnO donuts sensor at (a) 200 °C, (b) 250 °C, and (c) 300 °C and of the ZnO/rGO/ZnO donut sensor at (d) 200 °C, (e) 250 °C, and (f) 300 °C.

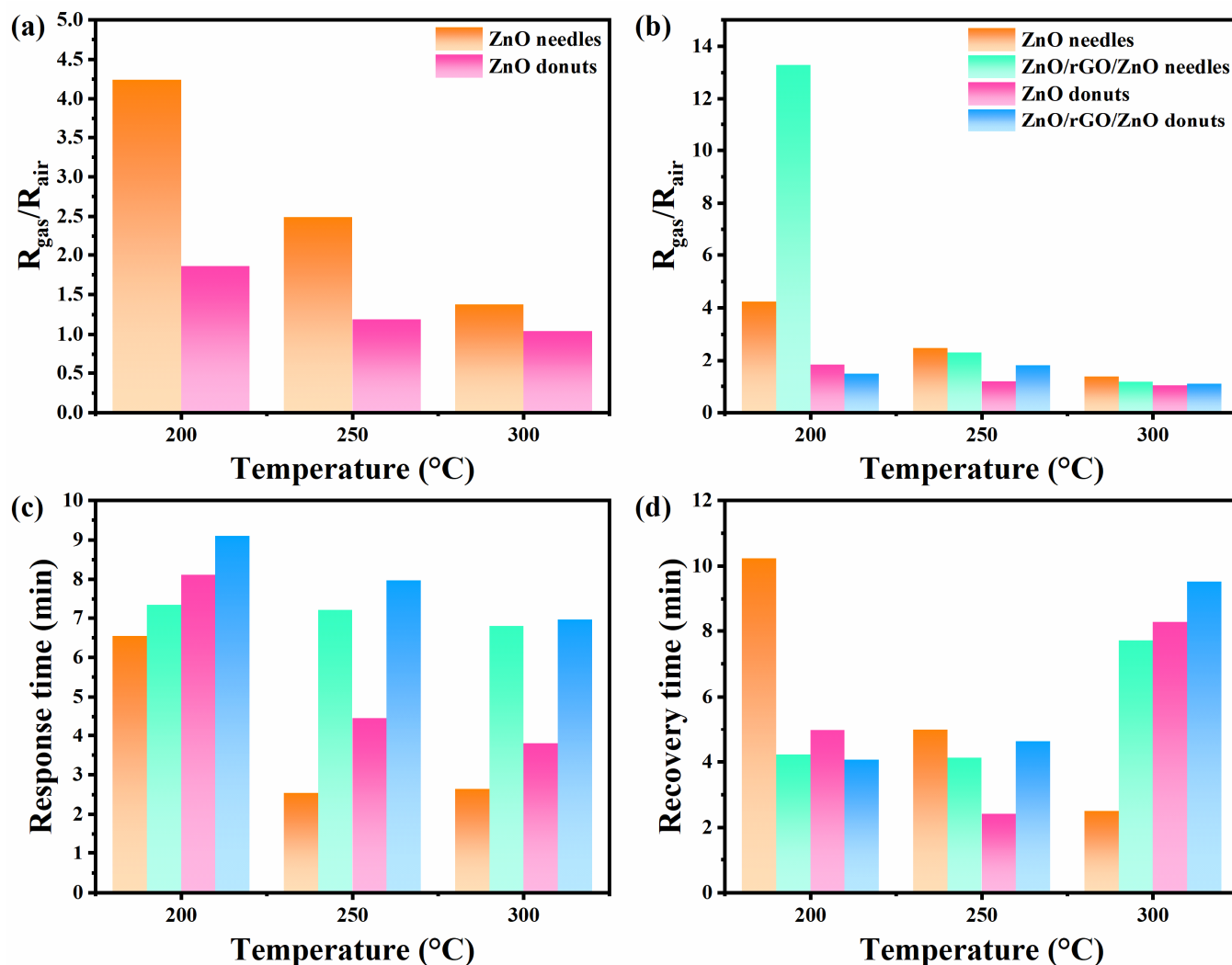


Figure 9. (a) Response ($R_{\text{gas}}/R_{\text{air}}$) of ZnO needle and donuts; (b) response ($R_{\text{gas}}/R_{\text{air}}$) of ZnO needle and donuts and their respective ZnO/rGO/ZnO composites; (c) response time and (d) recovery time of the ZnO needle-like and donut sensors and their respective ZnO/rGO/ZnO composites for 50 ppb O_3 at different operating temperatures.

Figure 9b displays the response of ZnO needle and donut sensors and their respective ZnO/rGO-ZnO composites, among which the ZnO/rGO/ZnO needle sensor showed a higher response compared to the ZnO/rGO/ZnO donut sensor at all evaluated temperatures (green and orange bars). Furthermore, a comparison of all sensors shows that the ZnO/rGO/ZnO needle exhibits a superior response at 200 °C due to the synergistic interaction between ZnO and rGO in the nanocomposite, where ZnO NPs act as a significant sensor material involved in gas adsorption and interaction with O_3 . Concomitantly, rGO provides more electrical channels for charge transport, directing the current through the nanocomposite and the electrode to obtain a better sensor response [60]. The interaction between the donut morphology and rGO seems to be weaker than for the needle morphology. The donuts have a much smaller particle size and tend to agglomerate more, forming compact clusters, as shown in Figure 4b,c. This agglomeration creates larger clusters of particles, diminishing the surface area [61] of the contact between the particles and the rGO sheets, which, in turn, reduces the interaction between them significantly, since the surface area is directly linked to reactivity and charge transfer effects [62,63]. Reduced contact and interaction between the composite components reduces charge transfer between the ZnO donuts and the rGO sheets, leading to a slight improvement in the sensor's characteristics.

Figure 9c shows the response time, defined as the time required to reach 90% of R_g (maximum resistance during exposure), for the sensors at different temperatures [17]. Compared to the ZnO needle and donut sensors, the former shows a shorter response time. The primary resistance to electron transport in the ZnO sensing layer is observed at the grain boundary barrier [64]. A comparison of the materials shows that ZnO needles and donuts exhibit similar crystallinity; however, the former displays a lower defect density, as indicated by Raman and PL results. Therefore, the depletion layer at the barrier is thinner, enabling electrons to be transferred more easily between grains. In addition, the needles have a unidirectional electron-transfer path, i.e., the shortest path, thereby achieving the fastest electron transmission speed [64]. A similar behavior is observed in ZnO/rGO/ZnO composites: the ZnO/rGO/ZnO needle composite shows shorter response times. Compared with pure ZnO, the sensors exhibited increased response time, which was not significant at the optimum operating temperature (200 °C). Following this methodology for manufacturing ZnO-rGO-ZnO composites with a “sandwich” structure, it is possible to optimize response/recovery times and thereby reduce the operating temperature of the sensors by varying the number of rGO layers in the composite. It is well known in the literature that rGO operates at low temperatures [65,66]. Figure 9d displays the recovery times of the sensors, defined as the time required to reach 10% of the baseline electrical resistance after gas shutoff [17]. A decrease in temperature results in shorter recovery times for the composite sensors (green and orange bars), suggesting that rGO reduces recovery times, as it can function as a gas sensor at low temperatures. A decrease in recovery time was observed at 250 °C for the ZnO donut-like sensor, followed by an increase when the temperature was further lowered to 200 °C. The ZnO needle-like sensor shows a decrease in recovery time as the temperature is lowered. According to such results, the ZnO/rGO/ZnO needle-like sensor displays the best properties for ozone sensing.

Figure 10a shows the response of the ZnO/rGO/ZnO needles sensor to different O_3 concentrations at 200 °C. Linear fitting of the response line vs. O_3 concentration yields the sensor's sensitivity (S), given by the slope of the line. Sensitivity was 0.09 ppb^{-1} for the ZnO/rGO/ZnO needle-like sensor. Figure 10b displays three consecutive cycles of exposure to 50 ppb O_3 at 200 °C. The ZnO/rGO/ZnO sensor can be adjusted and recovered to its initial state without any baseline drift after recovery. Figure 10c shows the stability of the ZnO/rGO/ZnO needles sample over time at 200 °C. The results indicate that the sensor is stable over long periods, as the response was similar when measured once a month during evaluations of the sensor's time stability. The sensor remains stable over long periods, since the response was consistent across all measurements. The sensor's selectivity was evaluated by exposing the sensor to four different gases, namely, two oxidizing ones (O_3 and NO_2) and two reducing ones (NH_3 and CO), and, according to Figure 10d, it shows a very low (or no) response to reducing gases and a higher selectivity to O_3 .

The donut morphology has a natural tendency to agglomerate, forming large clusters of particles, as shown in Figure 4b, with a decreased surface area. This results in a lower interaction between ZnO and rGO and more difficult dynamics for the adsorption/desorption mechanism. Moreover, the particle's shape is not ideal for fast electron transfer in comparison to the well-ordered stack of hexagonal planes (as in the needles morphology). Therefore, due to poorer interaction and hindered electron transfer between the donut morphology and the rGO sheets, the association between the donut morphology and the rGO might hinder charge transfer between the target gas and the composite, resulting in poorer responses and longer response and recovery times.

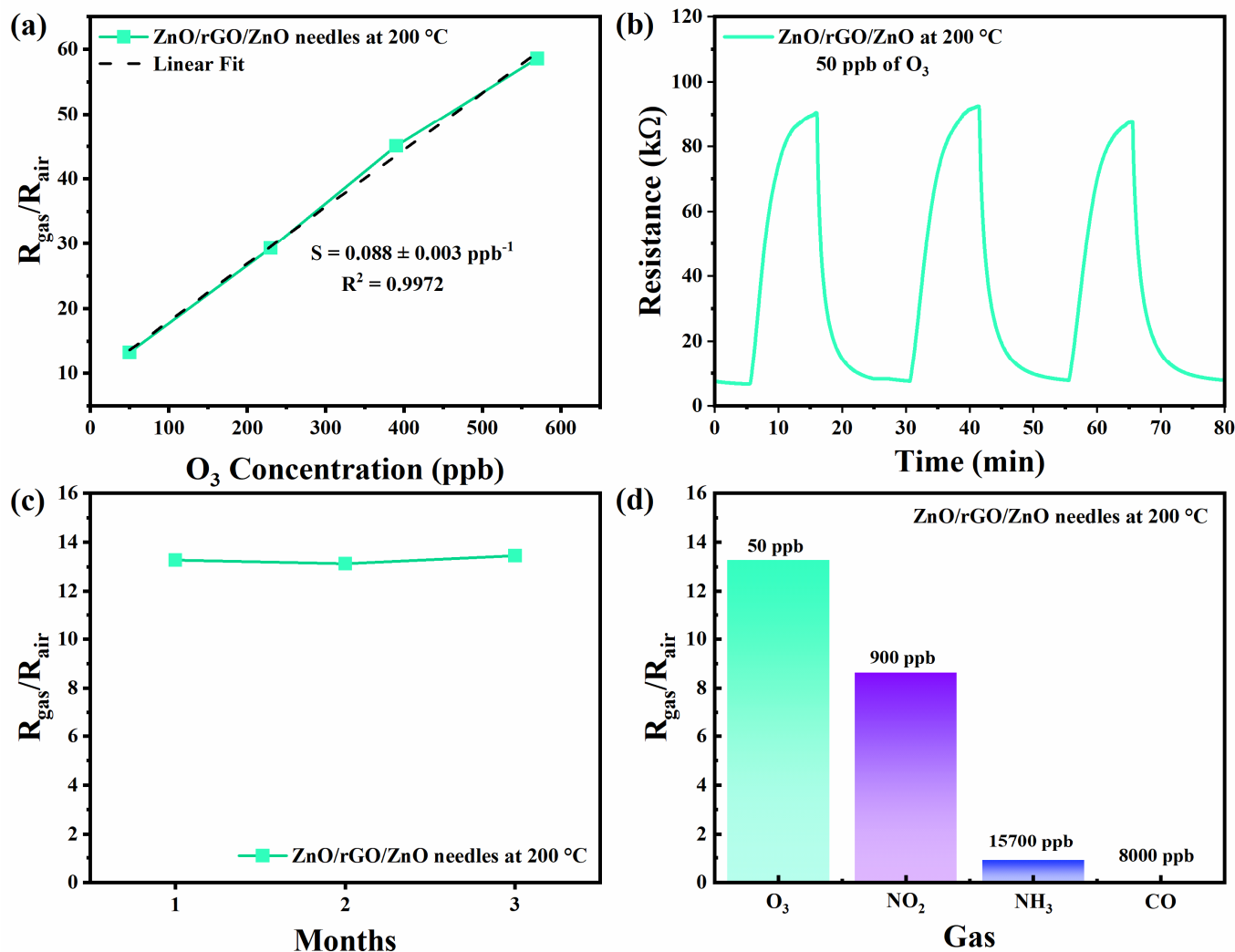


Figure 10. (a) Response of ZnO/rGO/ZnO needles sensor to different O_3 concentrations at 200 °C, (b) consecutive cycles of exposure to 50 ppb O_3 at 200 °C, (c) stability of ZnO/rGO/ZnO needles sensor for 50 ppb O_3 at 200 °C, and (d) selectivity of ZnO/rGO/ZnO needles sensor for O_3 , NO_2 , NH_3 , and CO gases at 200 °C.

Table 4 shows a comparison of the performance of the ZnO/rGO/ZnO needle-like sensor with that of sensors recently reported in the literature for ozone detection. The ZnO/rGO/ZnO sensor achieves good performance in detecting ozone gas at 200 °C, with excellent repeatability and selectivity at low O_3 concentrations, enabling detection below the WHO’s recommended limit (50 ppb over 8 h) [5].

Table 4. Sensing performance of the ZnO/rGO/ZnO needles ozone sensor compared with those previously published.

Sensing Materials	Concentration (ppb)	T (°C)	Response	Response/Recovery Time	Reference
ZnO/rGO/ZnO needles	50	200 °C	13.3 ^a	442/253	This work
rGO-ZnO	100	300 °C	49.6 ^a	-	[30]
ZnO-rGO-ZnO	135	250 °C	~37 ^a	498/360	[31]
CuO NWs	50	100 °C	40% ^b	-	[67]

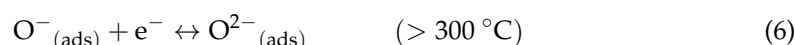
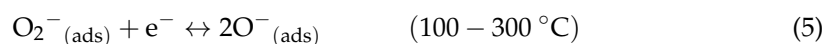
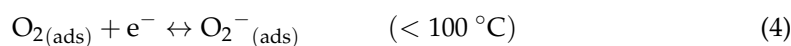
Table 4. Cont.

Sensing Materials	Concentration (ppb)	T (°C)	Response	Response/Recovery Time	Reference
In ₂ O ₃	200	70 °C	5 ^a	-	[13]
A-Fe ₂ O ₃	10	150 °C	~3.5 ^a	-	[68]
ZnO nanoporous	200	200 °C	216% ^b	300/600	[69]
In ₂ O ₃ -12	100	80 °C	16.7 ^a	707/422	[70]
β-In ₂ O ₃	40	160 °C	1.5 ^a	147/414	[71]

^a $R_{\text{gas}}/R_{\text{air}}$; ^b $(\Delta R/R_{\text{air}}) \times 100$.

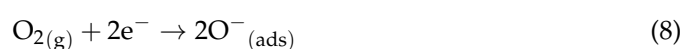
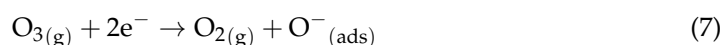
3.6. Gas Sensing Mechanisms

The gas-sensing mechanism of MOS is based on the adsorption of oxygen species on the sensor surface and on electron transfer [16]. Oxygen is adsorbed on the material surface as O₂⁻, O⁻, O²⁻ ions in function of temperature—Equations (3)–(6) [25].



The semiconductor type (p- or n-type) determines the sensor's detection mechanism. For an n-type, the mechanism depends on the carrier electrons, whereas in a p-type, it depends on the hole carrier density. Figure 11a shows the band structure of the pure materials. The formation of n- and p-type semiconductor composites affects sensor performance. The ZnO/rGO/ZnO sensor acts as an n-type semiconductor, with ZnO as the dominant semiconductor. rGO shows excellent electrical conductivity in the rGO/ZnO-based composite, providing a conductive path for efficient charge-carrier transport, whereas ZnO significantly contributes to achieving high sensor responses [60]. When the ZnO/rGO/ZnO composite is formed, electrons tend to flow from rGO regions to ZnO ones (p to n electron flow) towards balancing the Fermi level of the two materials, thus generating a potential barrier, which, created in the n-p composite by that charge transfer, causes energy band and energy level to bend (Figure 11b) [25,72]. When exposed to air at temperatures between 100 and 300 °C, adsorbed oxygen molecules extract electrons from the ZnO conduction band, forming O²⁻ species (Equation (5)) and increasing the potential barrier (space-charge layer), the depletion layer, and the curvature of the band. The phenomenon increases electrical resistance, since there are fewer electrons in the conduction band.

When the ZnO/rGO/ZnO composite comes into contact with O₃ gas, the gas molecules are adsorbed on ZnO and capture electrons from ZnO, thus causing electrons to be transferred from the ZnO/rGO/ZnO composite to the adsorbed O₃ on the surface and forming O⁻. The reaction can be represented by Equations (7) and (8) [33].



Due to the presence of an n-p junction in the ZnO/rGO/ZnO composite, the electrons captured in ZnO will be quickly supplied by the amount of electrons injected from rGO [25]. When the equilibrium state is reached, the width of the depletion layer between oxygen ions and ZnO increases, reducing the barrier between rGO and ZnO and ultimately increasing the hole density of the composite [1,25]. Besides providing a conductive pathway for charge

transport, rGO also has a very large surface area, offering a large number of active sites for gas adsorption. Regarding functional groups, introducing defect sites into pristine graphene increases adsorption energy, enabling interaction and charge transfer between rGO and the target gas, thereby allowing lower working temperatures and higher responses [61].

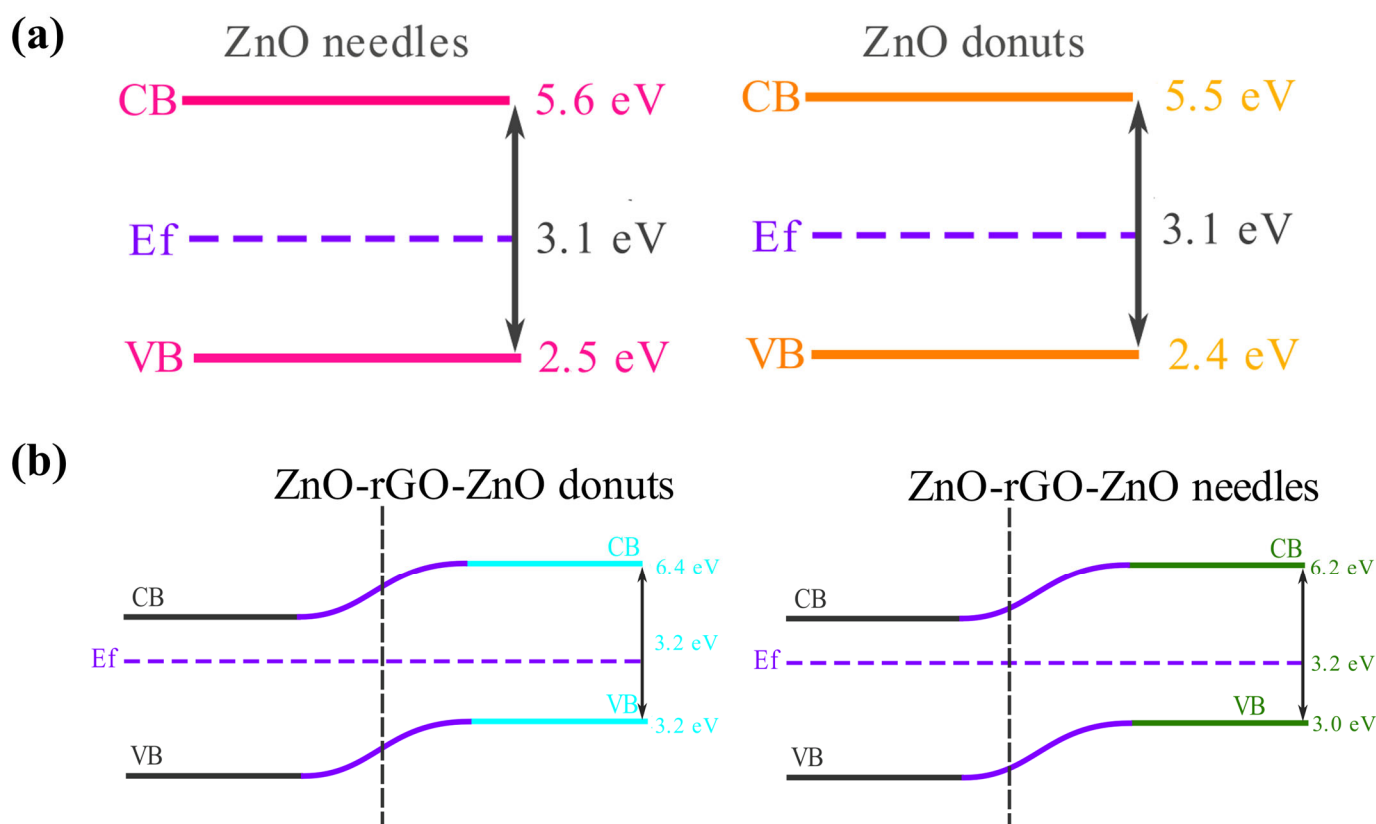


Figure 11. Band structure of samples of (a) ZnO and rGO and (b) ZnO-rGO-ZnO needles and ZnO-rGO-ZnO donuts.

Under ozone exposure, the efficient charge transfer at the composite interface modulates the band structure, resulting in a significant variation in sensor resistance [26]. Furthermore, rGO has oxygenated functional groups and additional structural defects, which provide more active sites for gas adsorption. On the other hand, the uniform distribution of ZnO NPs within the rGO sheets enhances the formation of more active adsorption sites for O₃. The presence of the n-p junction can also accelerate charge transfer, thereby improving the detection response [25].

4. Conclusions

ZnO/rGO/ZnO composites with needle and donut morphologies were fabricated according to the “sandwich” formation methodology for protecting rGO sheets during ozone exposure. ZnO/rGO/ZnO sensors showed no oxidation or degradation during ozone exposure, indicating that the adopted method protected rGO and potentially paving the way for the development of rGO/ZnO composite-based sensors for ozone detection. Among ZnO/rGO/ZnO composite sensors, the one with needle-like morphology displayed the best sensing properties, enabling detection of O₃ below the recommended detection limit. The ZnO/rGO/ZnO sensor exhibits a high response (R_{gas}/R_{air}) of 13.3 and recovery times of 442 s and 253 s, respectively, for 50 ppb of O₃, along with high selectivity for O₃ compared to other gases (NO₂, NH₃, and CO).

Supplementary Materials: The following supporting information can be downloaded at: <https://www.mdpi.com/article/10.3390/chemosensors14010010/s1>, Figure S1: Toxic gas detection system, Figure S2. Diffraction pattern of ZnO-rGO-ZnO samples with needle and donut morphology, Figure S3. Raman spectra of rGO sample, Figure S4. UV-Vis spectrum of ZnO needle and donut samples and their composites, Figure S5: FESEM images of rGO sample, Figure S6: (A) Diameter distribution and (B) width of ZnO donut NPs and (C) diameter distribution and (D) length of ZnO needle NPs, and Figure S7: High-resolution C 1s spectra of (A) ZnO/rGO/ZnO donut and (B) ZnO/rGO/ZnO needle samples, Figure S8. XPS Survey spectrum of ZnO-rGO-ZnO composites before and after O₃ exposure, Figure S9. High-resolution C 1s spectra of (A) ZnO/rGO/ZnO needles before O₃ exposure, (B) ZnO/rGO/ZnO needles after O₃ exposure, (C) ZnO/rGO/ZnO donuts before O₃ exposure and (D) ZnO/rGO/ZnO donuts after O₃ exposure, Table S1. Survey spectrum data of ZnO-rGO-ZnO composites before and after O₃ exposure, Table S2. High resolution C 1s spectral data of ZnO-rGO-ZnO composites before and after O₃ exposure.

Author Contributions: Conceptualization, A.A.K.; methodology, R.S.C., A.A.K., J.C.T. and N.C.S.P.; validation, A.A.K., R.S.C. and J.C.T.; formal analysis, A.A.K. and R.S.C.; investigation, R.S.C. and A.A.K.; resources, V.R.M.; writing—original draft preparation, A.A.K., R.S.C. and J.C.T.; writing—review and editing, N.C.S.P. and V.R.M.; visualization, A.A.K.; supervision, V.R.M.; project administration, V.R.M.; funding acquisition, V.R.M. All authors have read and agreed to the published version of the manuscript.

Funding: This research was funded by the São Paulo Research Foundation (FAPESP) (grants No 2013/07296-2, 2019/22076-5, 2022/03325-7, 2022/06404-5, 2022/07880-5, 2022/10340-2). Part of it was developed at the Brazilian Nanotechnology National Laboratory (LNNano) (Projects LMF-18580 and 20232214) in Campinas, SP, Brazil.

Data Availability Statement: The data presented in this study is available on request from the corresponding author.

Acknowledgments: The authors acknowledge the Brazilian National Science Foundation Agency (CNPq), CAPES, and Marcio Daldin Teodoro, from the Federal University of São Carlos, for the photoluminescence measurements.

Conflicts of Interest: The authors declare no conflicts of interest.

References

1. Ying, S.; Wang, Y.; Wu, Z.; Huang, M.; Dong, L.; Zhao, J.; Peng, C. Highly-Sensitive NO₂ Gas Sensors Based on Three-Dimensional Nanotube Graphene and ZnO Nanospheres Nanocomposite at Room Temperature. *Appl. Surf. Sci.* **2021**, *566*, 150720. [[CrossRef](#)]
2. Karakosta, E.S.; Karabagias, I.K.; Riganakos, K.A. Shelf Life Extension of Greenhouse Tomatoes Using Ozonation in Combination with Packaging under Refrigeration. *Ozone Sci. Eng.* **2019**, *41*, 389–397. [[CrossRef](#)]
3. Pandiselvam, R.; Subhashini, S.; Banuu Priya, E.P.; Kothakota, A.; Ramesh, S.V.; Shahir, S. Ozone Based Food Preservation: A Promising Green Technology for Enhanced Food Safety. *Ozone Sci. Eng.* **2019**, *41*, 17–34. [[CrossRef](#)]
4. Onofre, Y.J.; Catto, A.C.; Bernardini, S.; Fiorido, T.; Aguir, K.; Longo, E.; Mastelaro, V.R.; da Silva, L.F.; de Godoy, M.P.F. Highly Selective Ozone Gas Sensor Based on Nanocrystalline Zn_{0.95}Co_{0.05}O Thin Film Obtained via Spray Pyrolysis Technique. *Appl. Surf. Sci.* **2019**, *478*, 347–354. [[CrossRef](#)]
5. Ortega, P.P.; Palma, J.V.N.; Doimo, A.L.; Líbero, L.; Yamakawa, G.F.; Merízio, L.G.; Aguiar, E.C.; Silva, L.F.; Longo, E. Influence of Different Synthesis Methods on the Defect Structure, Morphology, and UV-Assisted Ozone Sensing Properties of Zinc Oxide Nanoplates. *Chemosensors* **2025**, *13*, 152. [[CrossRef](#)]
6. dos Santos Silva, W.A.; de Lima, B.S.; Bernardi, M.I.B.; Mastelaro, V.R. Enhancement of the Ozone-Sensing Properties of ZnO through Chemical-Etched Surface Texturing. *J. Nanoparticle Res.* **2022**, *24*, 96. [[CrossRef](#)]
7. Paralikis, A.; Gagaoudakis, E.; Kampitakis, V.; Aperathitis, E.; Kiriakidis, G.; Binas, V. Study on the Ozone Gas Sensing Properties of Rf-Sputtered Al-Doped NiO Films. *Appl. Sci.* **2021**, *11*, 3104. [[CrossRef](#)]
8. Belaqziz, M.; Amjoud, M.; Gaddari, A.; Rhouta, B.; Mezzane, D. Enhanced Room Temperature Ozone Response of SnO₂ Thin Film Sensor. *Superlattices Microstruct.* **2014**, *71*, 185–189. [[CrossRef](#)]
9. de Palma, J.V.N.; Catto, A.C.; de Oliveira, M.C.; Ribeiro, R.A.P.; Teodoro, M.D.; da Silva, L.F. Light-Assisted Ozone Gas-Sensing Performance of SnO₂ Nanoparticles: Experimental and Theoretical Insights. *Sens. Actuators Rep.* **2022**, *4*, 100081. [[CrossRef](#)]

10. Aguir, K.; Lemire, C.; Lollman, D.B. Electrical Properties of Reactively Sputtered WO₃ Thin Films as Ozone Gas Sensor. *Sens. Actuators B Chem.* **2002**, *84*, 1–5. [[CrossRef](#)]
11. Ding, J.; Xie, M.; Li, Z.; Wang, Y. Fabrication of WO₃ Nanosheets with Hexagonal/Orthorhombic Homo Junctions for Highly Sensitive Ozone Gas Sensors at Low Temperature. *J. Alloys Compd.* **2025**, *1010*, 178228. [[CrossRef](#)]
12. Resende Leite, R.; Komorizono, A.A.; Basso Bernardi, M.I.; Carvalho, A.J.F.; Mastelaro, V.R. Environmentally Friendly Synthesis of In₂O₃ Nano Octahedrons by Cellulose Nanofiber Template-Assisted Route and Their Potential Application for O₃ Gas Sensing. *Ceram. Int.* **2024**, *50*, 10192–10202. [[CrossRef](#)]
13. Sui, N.; Zhang, P.; Zhou, T.; Zhang, T. Selective Ppb-Level Ozone Gas Sensor Based on Hierarchical Branch-like In₂O₃ Nanostructure. *Sens. Actuators B Chem.* **2021**, *336*, 129612. [[CrossRef](#)]
14. Bejaoui, A.; Guerin, J.; Zapien, J.A.; Aguir, K. Theoretical and Experimental Study of the Response of CuO Gas Sensor Under Ozone. *Sens. Actuators B Chem.* **2014**, *190*, 8–15. [[CrossRef](#)]
15. Rocha, L.S.R.; Foschini, C.R.; Silva, C.C.; Longo, E.; Simões, A.Z. Novel Ozone Gas Sensor Based on ZnO Nanostructures Grown by the Microwave-Assisted Hydrothermal Route. *Ceram. Int.* **2016**, *42*, 4539–4545. [[CrossRef](#)]
16. Thomas, A.; Jeyaprakash, B.G. Selective Detection of Ammonia by RGO Decorated Nanostructured ZnO for Poultry and Farm Field Applications. *Synth. Met.* **2022**, *290*, 117140. [[CrossRef](#)]
17. Franco, M.A.; Conti, P.P.; Andre, R.S.; Correa, D.S. A Review on Chemiresistive ZnO Gas Sensors. *Sens. Actuators Rep.* **2022**, *4*, 100100. [[CrossRef](#)]
18. Wang, S.; Qiao, G.; Chen, X.; Wang, X.; Cui, H. Synthesis of ZnO Hollow Microspheres and Analysis of Their Gas Sensing Properties for N-Butanol. *Crystals* **2020**, *10*, 1010. [[CrossRef](#)]
19. Montero-Muñoz, M.; Ramos-Ibarra, J.E.; Rodríguez-Páez, J.E.; Marques, G.E.; Teodoro, M.D.; Coaquira, J.A.H. Growth and Formation Mechanism of Shape-Selective Preparation of ZnO Structures: Correlation of Structural, Vibrational and Optical Properties. *Phys. Chem. Chem. Phys.* **2020**, *22*, 7329–7339. [[CrossRef](#)] [[PubMed](#)]
20. Bolli, E.; Fornari, A.; Bellucci, A.; Mastellone, M.; Valentini, V.; Mezzi, A.; Polini, R.; Santagata, A.; Trucchi, D.M. Room-Temperature O₃ Detection: Zero-Bias Sensors Based on ZnO Thin Films. *Crystals* **2024**, *14*, 90. [[CrossRef](#)]
21. Gupta, S.; Ravikant, C.; Kaur, A. Facile Synthesis of Nitrogen-Doped Reduced Graphene Oxide/Zinc Oxide Nanocomposites for Enhanced Room-Temperature Ammonia Gas Detection. *J. Mater. Sci. Mater. Electron.* **2024**, *35*, 151. [[CrossRef](#)]
22. Pathak, A.; Samanta, S.; Bhangare, B.; Rajan, S.K.; Bahadur, J.; Ramgir, N.S.; Kaur, M.; Singh, A.; Debnath, A.K. Nanocomposites of ZnO Nanostructures and Reduced Graphene Oxide Nanosheets for NO₂ Gas Sensing. *ACS Appl. Nano Mater.* **2023**, *6*, 7649–7657. [[CrossRef](#)]
23. Li, D.; Lu, J.; Zhang, X.; Peng, X.; Li, J.; Yang, Y.; Hong, B.; Wang, X.; Jin, D.; Jin, H. Reversible Switching from P- to N-Type NO₂ Sensing in ZnO Rods/RGO by Changing the NO₂ Concentration, Temperature, and Doping Ratio. *J. Phys. Chem. C* **2022**, *126*, 14470–14478. [[CrossRef](#)]
24. Budhiraja, N.; Sapna, Kumar, V.; Tomar, M.; Gupta, V.; Singh, S.K. Facile Synthesis of Porous CuO Nanosheets as High-Performance NO₂ Gas Sensor. *Integr. Ferroelectr.* **2018**, *193*, 59–65. [[CrossRef](#)]
25. Chen, Z.; Guo, H.; Zhang, F.; Li, X.; Yu, J.; Chen, X. Porous ZnO/RGO Nanosheet-Based NO₂ Gas Sensor with High Sensitivity and Ppb-Level Detection Limit at Room Temperature. *Adv. Mater. Interfaces* **2021**, *8*, 2101511. [[CrossRef](#)]
26. Yuan, M.; Peng, C.; Fu, J.; Liu, X.; Wang, Z.; Xu, S.; Cui, S. High Surface Area ZnO/RGO Aerogel for Sensitive and Selective NO₂ Detection at Room Temperature. *J. Alloys Compd.* **2022**, *908*, 164567. [[CrossRef](#)]
27. Wang, B.; Bian, H.; Guo, M.; Tao, Z.; Luo, X.; Cui, Y.; Huang, J.; Tu, P. Low Temperature and High Sensitivity H₂S Gas Sensor Based on Ag/RGO/ZnO Ternary Composite Material. *Inorg. Chem. Commun.* **2025**, *180*, 114946. [[CrossRef](#)]
28. Sundaramoorthy, A.; Vivekananthan, V.; Hajra, S.; Panda, S.; Kim, H.J.; Nagarajan, N. A Flexible Nanocomposite Film Based on PVDF/ZnO-RGO for Energy Harvesting and Self-Powered Carbon Dioxide Gas Sensing. *Environ. Sci. Pollut. Res.* **2025**, *32*, 24325–24335. [[CrossRef](#)]
29. Jayachandiran, J.; Raja, A.; Arivanandhan, M.; Jayavel, R.; Nedumaran, D. A Facile Synthesis of Hybrid Nanocomposites of Reduced Graphene Oxide/ZnO and Its Surface Modification Characteristics for Ozone Sensing. *J. Mater. Sci. Mater. Electron.* **2018**, *29*, 3074–3086. [[CrossRef](#)]
30. De Lima, B.S.; Komorizono, A.A.; Silva, W.A.S.; Ndiaye, A.L.; Brunet, J.; Bernardi, M.I.B.; Mastelaro, V.R. Ozone Detection in the Ppt-Level with RGO-ZnO Based Sensor. *Sens. Actuators B Chem.* **2021**, *338*, 129779. [[CrossRef](#)]
31. Komorizono, A.A.; de Lima, B.S.; Mastelaro, V.R. Assessment of the Ozonolysis Effect of RGO-ZnO-Based Ozone Sensors. *Sens. Actuators B Chem.* **2023**, *397*, 134621. [[CrossRef](#)]
32. Groveman, S.; Peng, J.; Itin, B.; Diallo, I.; Pratt, L.M.; Greer, A.; Biddinger, E.J.; Greenbaum, S.G.; Drain, C.M.; Francesconi, L.; et al. The Role of Ozone in the Formation and Structural Evolution of Graphene Oxide Obtained from Nanographite. *Carbon* **2017**, *122*, 411–421. [[CrossRef](#)]
33. Tagliaferro, J.C.; Komorizono, A.A.; Pessoa, N.C.S.; Correia, R.S.; Bernardi, M.I.B.; Mastelaro, V.R. Influence of Morphology and Heterostructure Formation on the NO₂ Gas Sensing Properties of the ZnO-NiO System. *Talanta Open* **2024**, *10*, 100388. [[CrossRef](#)]

34. Cao, P.; Cai, Y.; Pawar, D.; Navale, S.T.; Rao, C.N.; Han, S.; Lu, Y. Down to Ppb Level NO₂ Detection by ZnO/RGO Heterojunction Based Chemiresistive Sensors. *Chem. Eng. J.* **2020**, *401*, 125491. [[CrossRef](#)]
35. Stobinski, L.; Lesiak, B.; Malolepszy, A.; Mazurkiewicz, M.; Mierzwa, B.; Zemek, J.; Jiricek, P.; Bieloshapka, I. Graphene Oxide and Reduced Graphene Oxide Studied by the XRD, TEM and Electron Spectroscopy Methods. *J. Electron Spectros. Relat. Phenomena* **2014**, *195*, 145–154. [[CrossRef](#)]
36. Beams, R.; Gustavo Cançado, L.; Novotny, L. Raman Characterization of Defects and Dopants in Graphene. *J. Phys. Condens. Matter* **2015**, *27*, 083002. [[CrossRef](#)]
37. Pimenta, M.A.; Dresselhaus, G.; Dresselhaus, M.S.; Cançado, L.G.; Jorio, A.; Saito, R. Studying Disorder in Graphite-Based Systems by Raman Spectroscopy. *Phys. Chem. Chem. Phys.* **2007**, *9*, 1276–1291. [[CrossRef](#)]
38. Kudin, K.N.; Ozbas, B.; Schniepp, H.C.; Prud'homme, R.K.; Aksay, I.A.; Car, R. Raman Spectra of Graphite Oxide and Functionalized Graphene Sheets. *Nano Lett.* **2008**, *8*, 36–41. [[CrossRef](#)]
39. Ferrari, A.C. Raman Spectroscopy of Graphene and Graphite: Disorder, Electron-Phonon Coupling, Doping and Nonadiabatic Effects. *Solid State Commun.* **2007**, *143*, 47–57. [[CrossRef](#)]
40. López-Díaz, D.; Delgado-Notario, J.A.; Clericò, V.; Diez, E.; Merchán, M.D.; Velázquez, M.M. Towards Understanding the Raman Spectrum of Graphene Oxide: The Effect of the Chemical Composition. *Coatings* **2020**, *10*, 524. [[CrossRef](#)]
41. Canado, L.G.; Takai, K.; Enoki, T.; Endo, M.; Kim, Y.A.; Mizusaki, H.; Jorio, A.; Coelho, L.N.; Magalhães-Paniago, R.; Pimenta, M.A. General Equation for the Determination of the Crystallite Size La of Nanographite by Raman Spectroscopy. *Appl. Phys. Lett.* **2006**, *88*, 163106. [[CrossRef](#)]
42. Arul, R.; Oosterbeek, R.N.; Robertson, J.; Xu, G.; Jin, J.; Simpson, M.C. The Mechanism of Direct Laser Writing of Graphene Features into Graphene Oxide Films Involves Photoreduction and Thermally Assisted Structural Rearrangement. *Carbon* **2016**, *99*, 423–431. [[CrossRef](#)]
43. Mrabet, S.; Ihzaz, N.; Bessadok, M.N.; Vázquez-Vázquez, C.; Alshammari, M.; El Mir, L. Microstructural, Raman, and Magnetic Investigations on Ca-Doped ZnO Nanoparticles. *J. Inorg. Organomet. Polym. Mater.* **2024**, *34*, 2064–2073. [[CrossRef](#)]
44. Achehboune, M.; Khenfouch, M.; Boukhoubza, I.; Leontie, L.; Doroftei, C.; Carlescu, A.; Bulai, G.; Mothudi, B.; Zorkani, I.; Jorio, A. Microstructural, FTIR and Raman Spectroscopic Study of Rare Earth Doped ZnO Nanostructures. *Mater. Today Proc.* **2021**, *53*, 319–323. [[CrossRef](#)]
45. Kumar, N.; Srivastava, A.K.; Patel, H.S.; Gupta, B.K.; Varma, G. Das Facile Synthesis of ZnO-Reduced Graphene Oxide Nanocomposites for NO₂ Gas Sensing Applications. *Eur. J. Inorg. Chem.* **2015**, *2015*, 1912–1923. [[CrossRef](#)]
46. Saikia, L.; Bhuyan, D.; Saikia, M.; Malakar, B.; Dutta, D.K.; Sengupta, P. Photocatalytic Performance of ZnO Nanomaterials for Self Sensitized Degradation of Malachite Green Dye under Solar Light. *Appl. Catal. A Gen.* **2015**, *490*, 42–49. [[CrossRef](#)]
47. Aldeen, T.S.; Ahmed Mohamed, H.E.; Maaza, M. ZnO Nanoparticles Prepared via a Green Synthesis Approach: Physical Properties, Photocatalytic and Antibacterial Activity. *J. Phys. Chem. Solids* **2022**, *160*, 110313. [[CrossRef](#)]
48. Abdolhosseinzadeh, S.; Asgharzadeh, H.; Sadighikia, S.; Khataee, A. UV-Assisted Synthesis of Reduced Graphene Oxide–ZnO Nanorod Composites Immobilized on Zn Foil with Enhanced Photocatalytic Performance. *Res. Chem. Intermed.* **2016**, *42*, 4479–4496. [[CrossRef](#)]
49. Jogi, A.; Ayana, A.; Rajendra, B.V. Modulation of Optical and Photoluminescence Properties of ZnO Thin Films by Mg Dopant. *J. Mater. Sci. Mater. Electron.* **2023**, *34*, 624. [[CrossRef](#)]
50. Murlidhar, G.; Kumar, R.; Kharat, P.B.; Khirade, P. Structural, Microstructural and Optical Characteristics of RGO-ZnO Nanocomposites via Hydrothermal Approach. *Opt. Mater.* **2024**, *154*, 115720. [[CrossRef](#)]
51. Akhter, S.; Lui, K.; Kung, H.H. Comparison of the Chemical Properties of the Zinc-Polar, the Oxygen-Polar, and the Nonpolar Surfaces of ZnO. *J. Phys. Chem.* **1985**, *89*, 1958–1964. [[CrossRef](#)]
52. Amin, G.; Asif, M.H.; Zainelabdin, A.; Zaman, S.; Nur, O.; Willander, M. Influence of PH, Precursor Concentration, Growth Time, and Temperature on the Morphology of ZnO Nanostructures Grown by the Hydrothermal Method. *J. Nanomater.* **2011**, *2011*, 269692. [[CrossRef](#)]
53. Yang, F.; Zhao, M.; Wang, Z.; Ji, H.; Zheng, B.; Xiao, D. The Role of Ozone in the Ozonation Process of Graphene Oxide: Oxidation or Decomposition? *RSC Adv.* **2014**, *4*, 58325–58328. [[CrossRef](#)]
54. Papadaki, D.; Mhlongo, G.H.; Motaung, D.E.; Nkosi, S.S.; Panagiotaki, K.; Christaki, E.; Assimakopoulos, M.N.; Papadimitriou, V.C.; Rosei, F.; Kiriakidis, G.; et al. Hierarchically Porous Cu-, Co-, and Mn-Doped Platelet-Like ZnO Nanostructures and Their Photocatalytic Performance for Indoor Air Quality Control. *ACS Omega* **2019**, *4*, 16429–16440. [[CrossRef](#)]
55. Ali, H.; Guler, A.C.; Masar, M.; Antos, J.; Hanulikova, B.; Urbanek, P.; Yasir, M.; Sopik, T.; Machovsky, M.; Kuritka, I. Structural Factors Influencing Photocatalytic and Photoelectrochemical Performance of Low-Dimensional ZnO Nanostructures. *Catal. Today* **2025**, *445*, 115088. [[CrossRef](#)]
56. Zhang, J.; Li, J.; Liu, X. Ternary Nanocomposite ZnO-g-C₃N₄-Go for Enhanced Photocatalytic Degradation of RhB. *Opt. Mater.* **2021**, *119*, 111351. [[CrossRef](#)]

57. Zhang, J.; Li, J. The Oxygen Vacancy Defect of ZnO/NiO Nanomaterials Improves Photocatalytic Performance and Ammonia Sensing Performance. *Nanomaterials* **2022**, *12*, 433. [[CrossRef](#)] [[PubMed](#)]
58. Platonov, V.; Malinin, N.; Vasiliev, R.; Rumyantseva, M. Room Temperature UV-Activated NO₂ and NO Detection by ZnO/RGO Composites. *Chemosensors* **2023**, *11*, 227. [[CrossRef](#)]
59. Yang, B.; Myung, N.V.; Tran, T.T. 1D Metal Oxide Semiconductor Materials for Chemiresistive Gas Sensors: A Review. *Adv. Electron. Mater.* **2021**, *7*, 2100271. [[CrossRef](#)]
60. Lu, J.; Li, D.; Chen, X.; Peng, X.; Li, J.; Yang, Y.; Hong, B.; Wang, X.; Jin, D.; Jin, H. ZnO/Reduced Graphene Oxide Nanocomposite with Synergic Enhanced Gas Sensing Performance for the Effective Detection of NO₂ at Room Temperature. *J. Nanoparticle Res.* **2022**, *24*, 265. [[CrossRef](#)]
61. Sett, A.; Majumder, S.; Bhattacharyya, T.K. Flexible Room Temperature Ammonia Gas Sensor Based on Low-Temperature Tuning of Functional Groups in Grapheme. *IEEE Trans. Electron Devices* **2021**, *68*, 3181–3188. [[CrossRef](#)]
62. Ariyoshi, K.; Tanimoto, M.; Yamada, Y. Electrochimica Acta Impact of Particle Size of Lithium Manganese Oxide on Charge Transfer Resistance and Contact Resistance Evaluated by Electrochemical Impedance Analysis. *Electrochim. Acta* **2020**, *364*, 137292. [[CrossRef](#)]
63. Ramakrishna, G.; Ghosh, H.N. Effect of Particle Size on the Reactivity of Quantum Size ZnO Nanoparticles and Charge-Transfer Dynamics with Adsorbed Catechols. *Langmuir* **2003**, *19*, 3006–3012. [[CrossRef](#)]
64. Wang, H.; Dai, M.; Li, Y.; Bai, J.; Liu, Y.; Li, Y.; Wang, C.; Liu, F.; Lu, G. The Influence of Different ZnO Nanostructures on NO₂ Sensing Performance. *Sens. Actuators B Chem.* **2021**, *329*, 129145. [[CrossRef](#)]
65. Chang, Y.S.; Chen, F.K.; Tsai, D.C.; Kuo, B.H.; Shieu, F.S. N-Doped Reduced Graphene Oxide for Room-Temperature NO Gas Sensors. *Sci. Rep.* **2021**, *11*, 20719. [[CrossRef](#)]
66. Modak, M.; Jagtap, S. Low Temperature Operated Highly Sensitive, Selective and Stable NO₂ Gas Sensors Using N-Doped SnO₂-RGO Nanohybrids. *Ceram. Int.* **2022**, *48*, 19978–19989. [[CrossRef](#)]
67. Lai, L.T.; Hsueh, H.T.; Chiu, C.H.; Cheng, T.C.; Chang, S.J. Thermal Oxidation CuO Nanowire Gas Sensor for Ozone Detection Applications. *Sens. Actuators Rep.* **2024**, *8*, 100228. [[CrossRef](#)]
68. Catto, A.C.; Bernardini, S.; Aguir, K.; Longo, E.; da Silva, L.F. In-Situ Hydrothermal Synthesis of Oriented Hematite Nanorods for Sub-Ppm Level Detection of Ozone Gas. *J. Alloys Compd.* **2023**, *947*, 169444. [[CrossRef](#)]
69. Nagarjuna, Y.; Hsiao, Y.J.; Wang, S.C.; Shao, C.Y.; Huang, Y.C. Nanoporous ZnO Structure Prepared by HiPIMS Sputtering for Enhanced Ozone Gas Detection. *Mater. Today Commun.* **2023**, *35*, 106024. [[CrossRef](#)]
70. Sui, N.; Zhang, P.; Cao, S.; Zhou, T.; Zhang, T. Nanosheet-Assembled In₂O₃ for Sensitive and Selective Ozone Detection at Low Temperature. *J. Alloys Compd.* **2021**, *888*, 161430. [[CrossRef](#)]
71. Souissi, R.; Bouguila, N.; Bendahan, M.; Aguir, K.; Fiorido, T.; Abderrabba, M.; Halidou, I.; Labidi, A. Ozone Sensing Study of Sprayed β-In₂S₃ Thin Films. *J. Alloys Compd.* **2022**, *900*, 163513. [[CrossRef](#)]
72. Khomarloo, N.; Mohsenzadeh, E.; Bagherzadeh, R.; Latifi, M.; Debliquy, M.; Ly, A.; Lahem, D.; Gidik, H. Fabrication of Gas Sensors for Detecting NO and NO₂ by Synthesizing RGO/ZnO Nanofibers. *J. Text. Inst.* **2025**, *116*, 3172–3182. [[CrossRef](#)]

Disclaimer/Publisher’s Note: The statements, opinions and data contained in all publications are solely those of the individual author(s) and contributor(s) and not of MDPI and/or the editor(s). MDPI and/or the editor(s) disclaim responsibility for any injury to people or property resulting from any ideas, methods, instructions or products referred to in the content.